ACCEPTED FOR PUBLICATION IN THE ASTROPHYSICAL JOURNAL
Preprint typeset using LATEX style emulateapj v. 11/10/09

arXiv:1105.3185v2 [astro-ph.HE] 10 Jun 2011

# DISCOVERY OF AN ENERGETIC PULSAR ASSOCIATED WITH SNR G76.9+1.0

Z. ARZOUMANIAN[1,2], E. V. GOTTHELF[3], S. M. RANSOM[4], S. SAFI-HARB[5], R. KOTHES[6], AND T. L. LANDECKER[6]

*Accepted for publication in The Astrophysical Journal*

## ABSTRACT

We report the discovery of PSR J2022+3842, a 24 ms radio and X-ray pulsar in the supernova remnant G76.9+1.0, in observations with the *Chandra* X-ray telescope, the Robert C. Byrd Green Bank Radio Telescope, and the *Rossi X-ray Timing Explorer* (*RXTE*). The pulsar's spin-down rate implies a rotation-powered luminosity $\dot{E} = 1.2 \times 10^{38}$ erg s$^{-1}$, a surface dipole magnetic field strength $B_s = 1.0 \times 10^{12}$ G, and a characteristic age of 8.9 kyr. PSR J2022+3842 is thus the second-most energetic Galactic pulsar known, after the Crab, as well as the most rapidly-rotating young, radio-bright pulsar known. The radio pulsations are highly dispersed and broadened by interstellar scattering, and we find that a large ($\delta f/f \approx 1.9 \times 10^{-6}$) spin glitch must have occurred between our discovery and confirmation observations. The X-ray pulses are narrow (0.06 cycles FWHM) and visible up to 20 keV, consistent with magnetospheric emission from a rotation-powered pulsar. The *Chandra* X-ray image identifies the pulsar with a hard, unresolved source at the midpoint of the double-lobed radio morphology of G76.9+1.0 and embedded within faint, compact X-ray nebulosity. The spatial relationship of the X-ray and radio emissions is remarkably similar to extended structure seen around the Vela pulsar. The combined *Chandra* and *RXTE* pulsar spectrum is well-fitted by an absorbed power-law model with column density $N_{\rm H} = (1.7 \pm 0.3) \times 10^{22}$ cm$^{-2}$ and photon index $\Gamma = 1.0 \pm 0.2$; it implies that the *Chandra* point-source flux is virtually 100% pulsed. For a distance of 10 kpc, the X-ray luminosity of PSR J2022+3842 is $L_{\rm X}(2\text{–}10~{\rm keV}) = 7.0 \times 10^{33}$ erg s$^{-1}$. Despite being extraordinarily energetic, PSR J2022+3842 lacks a bright X-ray wind nebula and has an unusually low conversion efficiency of spin-down power to X-ray luminosity, $L_{\rm X}/\dot{E} = 5.9 \times 10^{-5}$.

*Subject headings:* pulsars: individual (CXOU J202221.68+384214.8, PSR J2022+3842) — stars: neutron — supernova remnants — X-rays: stars

## 1. INTRODUCTION

The past decade has been witness to a highly productive back-and-forth relationship between X-ray and radio studies of supernova remnants (SNRs). Their nonthermal radio emissions, serving as tracers of particle acceleration, have motivated follow-up X-ray observations, most notably with the *Chandra* telescope. In many instances, X-ray imaging has revealed point-like sources surrounded by extended synchrotron structures, typically axisymmetric: these pulsar wind nebulae (PWNe) arise from the shocked outflows of relativistic particle winds driven by a central engine, the powerful time-varying fields in a neutron star magnetosphere. Targeted radio periodicity searches of PWNe have then uncovered previously unseen pulsations, providing the spin periods and, eventually, estimated ages, magnetic field strengths, and spin-down luminosities of the neutron stars, without which a meaningful physical understanding of the surrounding phenomena would be beyond reach. A few specific examples of this general picture of radio/X-ray symbiosis have been the discoveries of the pulsars in the remnants 3C58, G54.1+0.3, G292.0+1.8, and in the "Mouse" (see, e.g., Camilo 2004).

The Crab Nebula has been viewed for decades as a prototype, but there is growing evidence of PWNe with substantially different properties. At least three objects, among them the Vela SNR, have nonthermal radio spectra that are steep in comparison to the Crab (i.e., with spectral indices $\alpha \approx 0.6$, where flux $S_\nu \propto \nu^{-\alpha}$ at frequency $\nu$) and morphologies characterized by radio emission lobes straddling a central depression. While the nature of one such candidate PWN, DA 495, was once in question, X-ray imaging observations led to the discovery of an X-ray nebula and a presumed neutron star, both residing near the radio "hole" (Arzoumanian et al. 2008; hereafter, ASL+08). Radio and X-ray pulsation searches have not, however, detected a pulsar signature, so a key ingredient is lacking from our understanding of DA 495. In this paper, we describe a similar series of observations directed toward understanding the third member of this group of unusual SNRs, G76.9+1.0.

SNR G76.9+1.0 was discovered in a 408 MHz DRAO survey of the Cygnus X region and initially characterized as a "possible galactic object" (Wendker et al. 1991). Follow-up three-band radio observations using the Very Large Array (VLA) by Landecker et al. (1993) resolved a two-lobed structure 4′ in size, with a connecting bridge of emission, embedded in a faint, roughly circular emitting region 9′×12′ across. Based on its steep, nonthermal

---

Zaven.Arzoumanian@nasa.gov
[1] Center for Research and Exploration in Space Science and Technology and X-ray Astrophysics Laboratory, NASA Goddard Space Flight Center, Code 662, Greenbelt, MD 20771, USA
[2] Universities Space Research Association, Columbia, MD 21044, USA
[3] Columbia Astrophysics Laboratory, Columbia University, 550 West 120th Street, New York, NY 10027, USA
[4] National Radio Astronomy Observatory, 520 Edgemont Road, Charlottesville, VA 22901, USA
[5] Canada Research Chair. Department of Physics and Astronomy, University of Manitoba, Winnipeg, MB, R3T 2N2, Canada
[6] National Research Council of Canada, Herzberg Institute of Astrophysics, Dominion Radio Astrophysical Observatory, Box 248, Penticton, BC, V2A 6J9, Canada

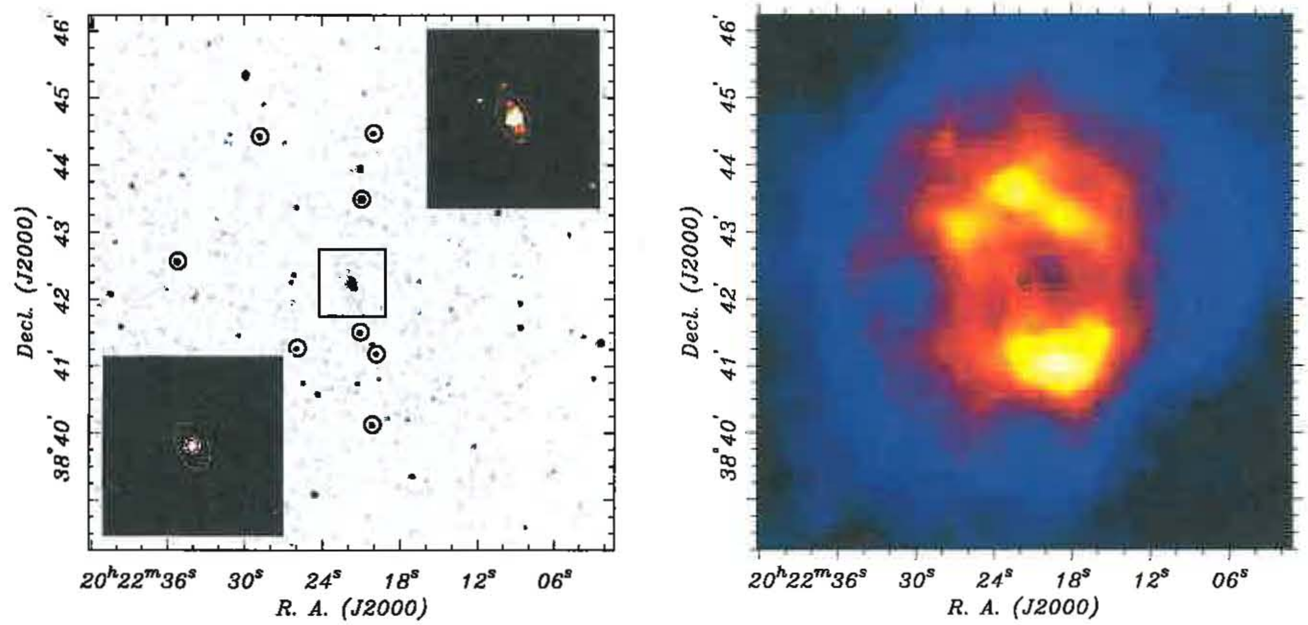

**Figure 1.** *Left:* *Chandra* ACIS-S3 0.5–7 keV X-ray image of the center of G76.9+1.0, smoothed, exposure-corrected, and scaled to emphasize the field point sources. The 1′ × 1′ box is centered on CXOU J202221.68+384214.8, while the circled sources were used to register the image. *Lower inset:* The unsmoothed count-rate map within the box containing the candidate neutron star and PWN. *Upper inset:* The result of adaptive smoothing of the same image. Overplotted are the regions used to extract spectral information for the unresolved source (*circle*) and diffuse emission (*ellipse*). *Right:* 1.49 GHz map of SNR G76.9+1.0 obtained using the VLA (see Landecker et al. 1993 for details) with the X-ray pulsar and nebula regions superposed (*contours*). The pulsar lies along the ridge of emission connecting the two lobes, adjacent to the central "hole." The arrangement is strikingly similar to the radio/X-ray configuration of the Vela pulsar and PWN (see Figure 10 of Dodson et al. 2003) as well as of DA 495 (Figure 1 of ASL+08).

spectrum, polarization, and morphological similarities to center-filled SNRs (in important respects such as the lack of an outer boundary and radially decreasing flux away from the central depression), these authors favored an SNR interpretation. In this picture, the radio lobes trace the Crab-like synchrotron emission of an evolved pulsar wind nebula.

Here we present imaging, spectral, and timing studies of G76.9+1.0 in X-rays and radio, culminating in the discovery of PSR J2022+3842 and of its associated X-ray PWN. In §2, we describe analysis of a *Chandra* observation that yielded the first identification of the SNR's central engine, a neutron star with its surrounding nonthermal nebula. In §3, we describe the discovery of the radio pulsar J2022+3842 and follow-up radio timing observations with the Green Bank Telescope (GBT) that have provided its spin-down rate and pulse properties. In §4, we present the results of a deep *Rossi X-ray Timing Explorer* (*RXTE*) observation: we show that the pulsed X-ray flux is consistent with the *Chandra* point-source flux, cementing the pulsar's association with the SNR.

For reasons developed below, we adopt a distance to G76.9+1.0 of 10 kpc throughout this work.

## 2. *Chandra* OBSERVATIONS AND RESULTS

SNR G76.9+1.0 was observed for 54 ks by the *Chandra* observatory on 2005 August 01 UT using the Advanced CCD Imaging Spectrometer (ACIS; Burke et al. 1997) operating in the full-frame TIMED/VFAINT exposure mode (ObsID #5586). This detector is sensitive to X-rays in the 0.3–12 keV energy range with a resolution of $\Delta E/E \sim 0.06$ FWHM at 1 keV. The CCD pixel scale is 0.5″, comparable to the telescope's on-axis spatial resolution. Low-level data were reprocessed with the latest calibrations using the CIAO script `chandra_repro`. The data analysis made use of the CIAO (V4.3), FTOOLS (V6.10), CALDB (V4.4.2), and XSPEC (V12.6.0q) software packages. A total of 53.7 ks of live-time was accumulated. No additional time filtering was necessary as the background rate was stable over the course of the observation. We followed the CIAO online science threads to create ACIS spectra and images. To allow for imaging with the best available angular resolution, we used the EDSER reprocessing option, applying an energy-dependent sub-pixel event-repositioning algorithm to each photon (Li et al. 2004).

The left-hand panel of Figure 1 presents the exposure-corrected image, in the 0.5–7 keV band, acquired by the ACIS-S3 and S2 CCDs, which together covered the entire extent of the radio SNR. No morphological evidence of G76.9+1.0 itself is apparent nor is there any hint of resolved diffuse emission in images created in the soft (< 2 keV) or hard (> 2 keV) energy bands; instead, several faint point-like sources are detected. The brightest of these, enclosed within a box in the figure, is located close to the optical axis and contains $N = 1190$ photons. This source is not associated with any known stellar counterpart or object in the 2MASS image of the field. Its identification as a possible neutron star associated with G76.9+1.0 is reinforced by the presence of faint but distinct X-ray nebulosity surrounding a brighter, unresolved core. To highlight the diffuse emission, we show as insets in Figure 1 both the raw and smoothed 0.5–7 keV count-rate maps for the boxed 1′ × 1′ region centered on the source. The smoothed image was produced using a circular convolution kernel of varying size, requiring a minimum of 5 counts within the kernel diameter. Although the putative nebula is faint, there is a clear excess of emission elongated on a line with position angle $\simeq 26^\circ$ North through East. This and the relative faintness of the point source argue against identification of the diffuse emission as a dust-scattering halo; these are normally circular and found around much brighter sources.

The 1.49 GHz Very Large Array (VLA) radio image shown in the right-hand panel of Figure 1 places the X-ray nebula in the context of the double-lobed radio structure. The unambiguous alignment of the long axis of the diffuse X-ray emission with the radio ridge connecting the lobes suggests that the radiation processes underlying the emissions in both bands are related, such as in the canonical picture of synchrotron emission from relativistic particles originating in the pulsar's magnetosphere.

To refine the location of the putative pulsar, the X-ray image was registered using the coordinates of eight 2MASS infrared counterparts obtained from the NASA/IPAC Infrared Science Archive. The updated centroid is located at (J2000.0) R.A. = $20^{\rm h}22^{\rm m}21^{\rm s}.689$, Decl. = $+38^\circ42'14''.82$ with a $1\sigma$ uncertainty of $(0''.09, 0''.07)$ in the two coordinates, respectively. The required shift in R.A. and Decl. was $(-0''.012, -0''.162)$. This source, CXOU J202221.68+384214.8, is hereafter referred to by the shortened name CXOU J202221.

We extracted a spectrum for CXOU J202221, and generated an appropriate response matrix, with the `specextract` CIAO script, using a circular $2''.5$-radius aperture (representing > 90% encircled energy, depending on photon energy) centered on the source. The diffuse emission and cosmic and detector backgrounds contribute negligibly ($\sim 10$ counts) in this region. With a maximum count rate in a pixel of $< 4 \times 10^{-3}$ s$^{-1}$, photon pile-up could safely be ignored. The 0.5–10 keV spectrum was grouped with a minimum of 15 counts per spectral channel and fitted using XSPEC to an absorbed power-law model, a common property of young, rotation-powered pulsars. (Blackbody models are formally allowed, but produce unnaturally high temperatures.) An excellent fit, with $\chi^2 = 69.5$ for 70 degrees of freedom (DoF) was obtained for an absorbing column $N_{\rm H} = (1.6 \pm 0.3) \times 10^{22}$ cm$^{-2}$ and photon index $\Gamma = 1.0 \pm 0.2$ (90% confidence intervals are used throughout). The absorbed 2–10 keV source flux is $F_{\rm PSR} = 5.3 \times 10^{-13}$ erg cm$^{-2}$ s$^{-1}$, implying an isotropic luminosity of $L_{\rm X} = 7.0 \times 10^{33}$ erg s$^{-1}$ at 10 kpc distance. As described in §4.2, this *Chandra* spectrum was also used in joint fits with *RXTE* data.

To investigate the spectrum of the nebula, we used an elliptical extraction region (Figure 1), with semi-major and -minor axes of length $8''.3 \times 5''.1$, centered on the pulsar, with the point-source region ($r < 2''.5$) excluded. For the local background, we extracted photons from a concentric annular region well outside the nebular extent ($20'' < r < 40''$). We also performed a `MARX` simulation to determine the small (2.6%) flux contribution within the nebular region from point-source photons scattered into the point-spread function wings; this simulation took into account the measured pulsar spectrum. The tally of background-subtracted counts from the nebula is then $N = 76 \pm 13$. The faintness of the nebula does not allow a well-constrained spectral fit; instead we fixed the column density to the best-fit value for the unresolved source and assumed a nominal absorbed power-law model with $\Gamma = 1.4$, a value derived from the empirical trend relating the spectral indices of energetic pulsars and their nebulae (Gotthelf 2004). The absorbed 2–10 keV flux for the putative PWN is $F_{\rm PWN} \approx 4 \times 10^{-14}$ erg cm$^{-2}$ s$^{-1}$. The flux ratio $F_{\rm PWN}/F_{\rm PSR} \approx 0.08$ is well below that expected for similarly energetic pulsars (Gotthelf 2004). The uncertainty in this result is dominated by the small number of nebula photons and not the choice of $\Gamma$.

## 3. RADIO OBSERVATIONS AND RESULTS

Motivated by the *Chandra* discovery of the point source and possible PWN at the heart of SNR G76.9+1.0, we searched for radio pulsations with the GBT. The Spectrometer SPIGOT data-acquisition backend (Kaplan et al. 2005) was used for 5 hours on each of two days, with 600 MHz of useful bandwidth centered at 1.95 GHz. The instrument provided 768 channels with 16-bit sampling of summed polarizations at 81.92 $\mu$s intervals. The PRESTO software (Ransom et al. 2002) was used to search for pulsations, and a candidate 24-ms periodicity was detected on both days with formal significances of $7\sigma$ on MJD 54397 and $12\sigma$ on MJD 54400. Confirmation observations were carried out on 2009 May 6 (MJD 54957) using the GUPPI data-acquisition system configured similarly to the discovery instrumentation, but with the addition of full-Stokes sensitivity. The difference in the pulse periods derived at these epochs gave the first indication of the pulsar's spin-down rate and thence its canonical age, magnetic field strength, and spin-down power (see below). A search for single "giant" pulses yielded no compelling candidates, despite the fact that the pulsar's estimated magnetic field strength at the light cylinder, suggested to be relevant in the production of giant pulses (Cognard et al. 1996), is approximately 70% that of both the Crab pulsar and PSR B1937+21, and comparable to that of PSR B1821−24, all of which exhibit giant pulses.

Additional radio observations, also with the GUPPI system, were carried out at roughly 3-month intervals to constrain the pulsar's long-term timing behavior. Notably, the pulse periods measured during and after the confirmation observation differed substantially from those detected during the two discovery observations made 1.5 years earlier, implying that a spin "glitch" of magnitude $\Delta P/P \simeq 1.9 \times 10^{-6}$ had occurred at an unknown epoch in this interval. The spacing of the radio timing observations together with apparent "timing noise" instability in the pulsar's rotation on similar timescales precluded derivation of a phase-connected timing solution. We therefore determined the long-term average spin-down rate, $4.3192(27) \times 10^{-14}$, through a least-squares fit to the multi-epoch period measurements (Figure 2), a result consistent with the short-term X-ray-derived ephemeris shown in Table 1 (see §4.1).

The pulsar's flux density at 2 GHz, $S_{2\,{\rm GHz}}$, is 60 $\mu$Jy; its 4.8 GHz flux density of $\approx 45$ $\mu$Jy suggests that PSR J2022+3842 has an unusually flat spectrum, $\alpha \simeq -0.33$. The implied radio pseudo-luminosity

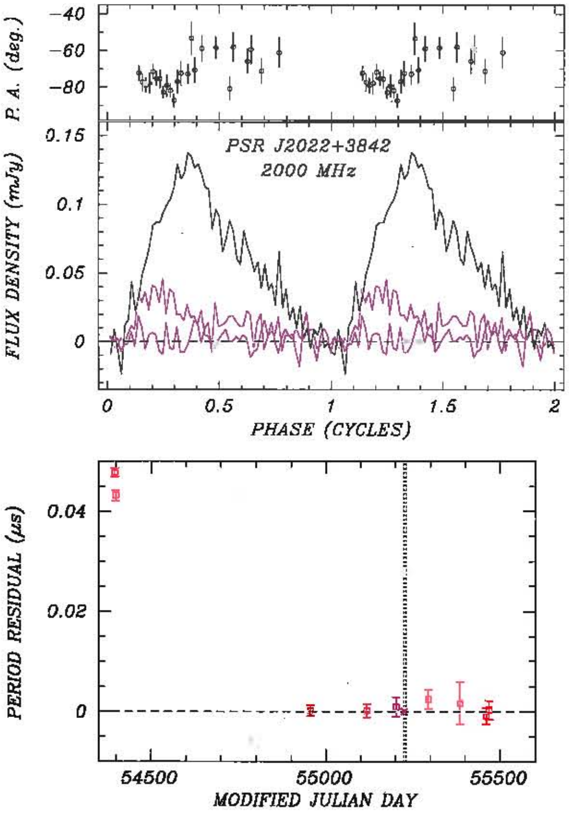

**Figure 2.** *Top:* Radio pulse properties of PSR J2022+3842 averaged over a 700 MHz band centered at 1.95 GHz, and representing a total integration time of approximately 24 hours. The evolution with pulse phase of total (*black line*), linearly polarized (*red*), and circularly polarized (*blue*) flux are shown. Phase zero is arbitrary. *Bottom:* Radio pulse period evolution (*red squares*) with $1\sigma$ uncertainty error bars; the blue cross corresponds to the *RXTE* observation (uncertainty much smaller than the plotted symbol). Residuals are relative to the timing model shown in Table 1. The pulse period at the discovery epoch of the radio pulsations, around MJD 54400, was significantly longer than at later times, indicating that a spin-up glitch occurred at some point before the confirmation observation near MJD 54950.

$S_{1.4\,\mathrm{GHz}} d^2 \simeq 7\,D_{10}^2$ mJy kpc$^2$ is unremarkable, low in comparison to the majority of known pulsars, but an order of magnitude higher than the luminosities of other young, faint pulsars discovered in deep searches of SNRs (Camilo 2004). Even with a long cumulative exposure, our best average pulse profile (Figure 2) retains significant statistical noise; despite this faintness, a number of relevant pulse shape and polarization results are available.

The radio pulsations of PSR J2022+3842 are significantly affected by dispersion and scattering due to propagation in the interstellar medium, which are typically important at frequencies $\lesssim 1$ GHz, even in our 2 GHz observations. To estimate dispersion measure (DM) and the pulse broadening timescale $\tau^{\mathrm{scatt}}$, we formed a pulse-shape model assuming a gaussian-shaped intrinsic profile, a one-sided exponential-decay impulse response function for the scatter-broadening, and a $\nu^{-4}$ frequency dependence for the width of the exponential. We fit the S-band (i.e., 2 GHz) data to this model in four evenly-spaced frequency sub-bands, allowing the width of the intrinsic gaussian profile to vary and also accounting for a DM bias caused by the frequency-dependent pulse broadening due to scattering. This simple model fit the data well, but we caution that the assumptions inherent in the model may introduce significant systematic errors, perhaps as large as twice the statistical uncertainties quoted below.

The NE2001 Galactic electron distribution model (Cordes & Lazio 2002) fails to accommodate the derived DM $= 429.1 \pm 0.5$ pc cm$^{-3}$ in the direction of PSR J2022+3842—formally, the model suggests a lower bound on the distance to the pulsar of 50 kpc. Instead, a likely over-density of free electrons in the Cygnus region, along the line of sight, accounts for the higher-than-expected dispersion—a similar explanation has been advanced for the unexpectedly large DM of the nearby PSR J2021+3651 (Roberts et al. 2002).

In this direction, the Perseus Arm lies at a distance of approximately 6 kpc, and the Outer Arm at $\gtrsim 10$ kpc. For convenience in scaling distance-dependent parameters and because the larger distance brings X-ray efficiencies more approximately in line with those of other young pulsars (see §5), we adopt a distance $d = 10\,D_{10}$ kpc. Independent supporting evidence for the large distance derives from H I absorption and X-ray studies of the PWN CTB 87 (Kothes et al. 2003), roughly 2° from G76.9+1.0 on the sky. At a distance of 6.1 kpc, CTB 87 lies in the Perseus arm and its X-ray-derived absorbing column is $N_{\mathrm{H}} = (1.4 \pm 0.2) \times 10^{22}$ cm$^{-2}$ at 90% confidence (Safi-Harb, Matheson & Kothes, in preparation); although their uncertainties are large, the nominal H I column for G76.9+1.0 is somewhat larger than that for CTB 87. A radio bright extragalactic point source adjacent to CTB 87 exhibits a deep absorption component at a velocity of about $-85$ km s$^{-1}$ not seen in the absorption profile of CTB 87. This feature could account for the larger foreground absorption toward G76.9+1.0 if the latter is located at a significantly larger distance, such as the Outer Arm or beyond it.

The NE2001 model also predicts a timescale for pulse broadening due to interstellar scattering of 0.3 ms at 1 GHz; instead, we find $\tau^{\mathrm{scatt}}_{1\mathrm{GHz}} = 55 \pm 7$ ms, which scales to 3.8 ms at the center of our observing band but varies strongly across it. The long decay of the pulse, here averaged over the 700 MHz band, can be seen in the upper half of Figure 2. Consistent with this result, an exploratory observation centered at 800 MHz sky frequency failed to detect the pulsar; similar attempts at 1.4 GHz and 5 GHz yielded weak detections. At 5 GHz, the pulse was unexpectedly broad, consistent with the results of the frequency-subband fit to the pulse shape. Thus, in addition to the importance of scatter-broadening at the lower frequencies, the pulse appears to be intrinsically broad, roughly 30% of the pulse period, full width at half maximum. The well-established trend of pulse widths increasing as $P^{-0.5}$ underestimates this result by a factor of 2–3 (e.g., for the outermost conal component of Mitra & Deshpande 1999).

Polarization calibration and analysis using the PSRCHIVE software package (Hotan et al. 2004) reveals that the radio pulse is substantially linearly polarized, despite the depolarizing effects of multipath propagation in the scattering tail, incomplete removal of Faraday rotation (due to the low signal-to-noise ratio), and other effects. The true polarized fraction in the pulse is likely to be significantly larger than we have observed. The variation of the polarization vector's position angle with rotational phase, shown in the top-most panel of Figure 2, is found to be fairly flat, inconsistent with the canonical rotating-vector model (Radhakrishnan & Cooke 1969), but similar to behavior seen in the Crab pulsar (especially its high-frequency components; Moffett & Hankins 1999) and several millisecond-period "recycled" pulsars (Ord et al. 2004). Perhaps not coincidentally, many of these same pulsars exhibit nonthermal magnetospheric pulsations in X-rays. Finally, we note that the pulsar's rotation measure is RM $\simeq +270$ rad m$^{-2}$.

## 4. *RXTE* OBSERVATIONS AND RESULTS

The field containing CXOU J202221 was observed by *RXTE* for a total of 99 ks over the 8-day span 2010 January 27–February 4 UT (observation P95316). The data were collected with the Proportional Counter Array (PCA; Jahoda et al. 1996) in the GoodXenon mode with an average of 1.8 of the 5 proportional counter units (PCUs) active. In this mode, photons are time-tagged to 0.9 $\mu$s and have an absolute uncertainty better than 100 $\mu$s (Rots et al. 1998). The effective area of five combined detectors is approximately 6500 cm$^2$ at 10 keV with a roughly circular field-of-view of $\sim 1^\circ$ FWHM. Spectral information is available in the 2–60 keV energy band with a resolution of $\sim 16\%$ at 6 keV.

Production PCA data for this observation were obtained from NASA's HEASARC archive and time-filtered using the standard criteria. This rejected intervals of South Atlantic Anomaly passages, Earth occultations, and other periods of high particle activity, resulting in a total of 94.2 ks of useful data. The photon arrival times were transformed to the solar system barycenter in Barycentric Dynamical Time (TDB) using the JPL DE200 ephemeris and the *Chandra*-derived coordinates of CXOU J202221.

### 4.1. *Timing Analysis*

The timing analysis was restricted to PCA channels 2–50, corresponding approximately to the 2–20 keV energy range, and from the top Xenon layer of each PCU, to optimize the signal-to-noise for a typical pulsar spectrum. Because of the long observation span, photon detection times were accumulated in 4-ms bins and a $2^{28}$-point accelerated Fast Fourier Transform (FFT) was performed to search for a periodic signal, testing a range of plausible frequency derivatives. This immediately revealed a signal at 24 ms of sufficient strength to analyze short intervals of data and build up a fully phase-coherent timing solution using the time of arrival (TOA) method, as follows.

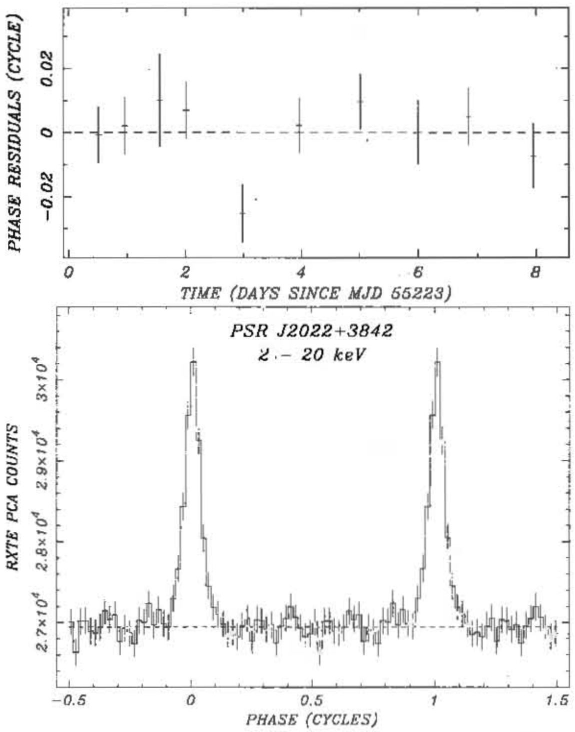

**Figure 3.** *RXTE* timing results for PSR J2022+3842 in the 2–20 keV X-ray band. *Top:* Phase residuals after fitting the phase-connected quadratic ephemeris given in Table 1 to the set of PCA observations as described in §4.1. On average, individual TOA measurements were obtained in 17 ks-PCU of exposure. *Bottom:* The pulse profile of the *RXTE* data folded on the best-fit ephemeris. Two cycles are shown for clarity.

The *RXTE* observations of CXOU J202221 distributed over the 8 days were clustered into 10 groups of two, three, or four adjacent 96-min orbits, with large gaps in between. For each of these groups, we were able to extract the period and phase of the signal with sufficiently small uncertainties to maintain cycle counts between fitted epochs. Pulse profiles were generated using the optimum period derived from the $Z_n^2$ test (Buccheri et al. 1983) with $n = 10$ harmonics to allow for the sharp profile. The resulting profiles were cross correlated, shifted, and summed to generate a master pulse profile template. Individual profiles were then cross-correlated with the template to determine the arrival time (time of phase zero) and its uncertainty at each epoch.

The derived TOAs were iteratively fitted to a quadratic ephemeris using the TEMPO software. We started by fitting TOAs from the first three most closely spaced TOAs to a linear solution, and then iteratively added the next TOA. At each step we found that the new TOA would match to $< 0.02$ cycles the predicted phase derived from the previous set. The resulting ephemeris referenced to the mid-point of the observation is presented in Table 1 and the phase residuals are shown in Figure 3. The residuals are all less than 0.02 cycles and appear to be random within their statistical uncertainties, with the exception of a single $3\sigma$ data point ($\Delta\phi = 0.025 \pm 0.01$) which an investigation finds no reason to exclude.

Figure 3 displays the pulse profile using all of the 2–20 keV data folded on the final ephemeris. It has a single symmetric peak that is triangular in shape and narrow, with a FWHM of 0.06 of a full cycle. The measured pulsed emission corresponds to 0.91% of the total PCU countrate; however, as will be shown below, the intrinsic signal is nearly 100% pulsed compared to the flux derived from the spectrum of CXOU J202221. We see no energy

**Table 1**
Properties of PSR J2022+3842

| Parameter | Value |
|---|---|
| *X-ray Measurements* | |
| R.A. (J2000)[a] | $20^{\mathrm{h}}22^{\mathrm{m}}21\overset{\mathrm{s}}{.}689(6)$ |
| Decl. (J2000)[a] | $+38^{\circ}42'14\overset{''}{.}82(7)$ |
| Epoch (MJD TDB)[b] | 55227.00000027 |
| Period, $P$ (ms)[b] | 24.2877561082(84) |
| Period derivative, $\dot{P}$[b] | $4.3064(93) \times 10^{-14}$ |
| Range of timing solution (MJD)[b] | 55223–55231 |
| *Radio Measurements* | |
| Long-term average $\dot{P}$ | $4.3192(27) \times 10^{-14}$ |
| Range of $\dot{P}$ fit (MJD) | 54957–55469 |
| Dispersion measure, DM (pc-cm$^{-3}$) | $429.1 \pm 0.5$ |
| Scatter-braodening timescale, $\tau^{\mathrm{scatt}}_{1\,\mathrm{GHz}}$ (ms) | 55(7) |
| Flux density, $S_{2\,\mathrm{GHz}}$ ($\mu$Jy) | 60 |
| *Derived Parameters* | |
| Characteristic age, $\tau_c$ (kyr) | 8.9 |
| Spin-down luminosity, $\dot{E}$ (erg s$^{-1}$) | $1.19 \times 10^{38}$ |
| Surface dipole magnetic field, $B_s$ (G) | $1.03 \times 10^{12}$ |

**Note.** — $1\sigma$ uncertainties given in parentheses.

[a] *Chandra* ACIS-S3 position registered using 2MASS objects (see text).

[b] *RXTE* phase-connected ephemeris.

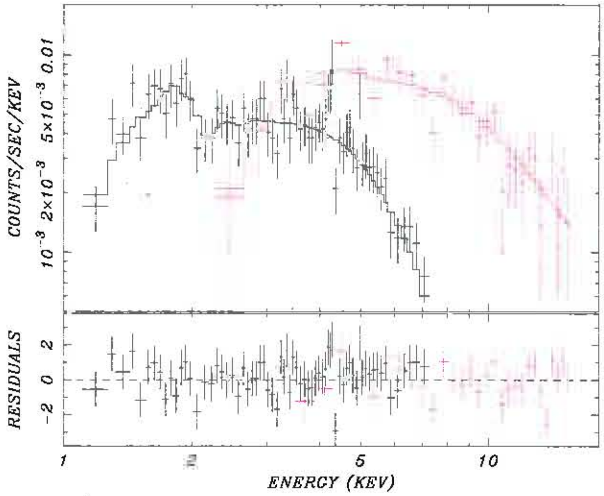

**Figure 4.** The *Chandra* ACIS spectrum of CXOU J202221 (*black*) and the *RXTE* PCA spectrum of the pulsed emission from PSR J2022+3842 (*red*), fitted jointly to an absorbed power-law model, with independent normalizations. The solid line shows the best-fit model (see text §4.2). The pulsed *RXTE* flux is obtained by subtracting the off-peak spectrum from the on-peak spectrum. Residuals from the best fit are shown in units of standard deviation.

dependence of the pulse profile when subdividing the 2–20 keV *RXTE* energy range.

### 4.2. *RXTE Spectral Analysis*

The pulsed-flux spectrum of PSR J2022+3842 can be isolated through phase-resolved spectroscopy. We used the FTOOLS `fasebin` software to construct phase-dependent spectra based on the ephemeris of Table 1. We combined spectra from all observation intervals using only data recorded in the top Xenon layer of PCU#2; this PCU was (uniquely) used for all observation intervals over the 8 days. Similarly, we averaged the standard PCA responses generated for each epoch. In fitting the pulsed flux, the unpulsed emission provides a near perfect background estimate. The spectra were accumulated in two phase intervals representing the off-peak ($0.1 < \phi_{\mathrm{off}} \leq 0.88$) and on-peak ($0.88 < \phi_{\mathrm{on}} \leq 1.1$) emission and fitted using XSPEC. The fits were performed in the 2–16 keV range, above which the background dominates.

Based on the *Chandra* spectrum, we fitted an absorbed power-law model with the interstellar absorption held fixed at $N_{\mathrm{H}} = 1.6 \times 10^{22}$ cm$^{-2}$; leaving $N_{\mathrm{H}}$ unconstrained results in a larger uncertainty in $\Gamma$. The resulting best-fit photon index is $\Gamma = 1.1 \pm 0.2$ with $\chi^2 = 27.9$ for 30 DoF. The absorbed 2–10 keV flux for the pulsed emission is $5.4 \times 10^{-13}$ erg cm$^{-2}$ s$^{-1}$, which represents all of the point-source flux measured from CXOU J202221, indicating that its intrinsic pulsed fraction is essentially 100%. In Figure 4, we show the result of a joint fit to the *RXTE* pulsed emission from PSR J2022+3842 and CXOU J202221 in the 0.5–16 keV band, leaving only their normalizations free. The best fit parameters are $N_{\mathrm{H}} = (1.7 \pm 0.3) \times 10^{22}$ cm$^{-2}$ and $\Gamma = 1.0 \pm 0.2$ with $\chi^2 = 99.3$ for 100 DoF. There is no indication of spectral curvature in the fitted energy range. The independently measured absorbed 2–10 keV flux is the same for both CXOU J202221 and the pulsed emission from PSR J2022+3842, namely $F_X = 5.3 \times 10^{-13}$ erg cm$^{-2}$ s$^{-1}$. We adopt the results of the joint spectral fit as our final reported values.

## 5. DISCUSSION

There can be little doubt that CXOU J202221 and PSR J2022+3842 are one and the same: the non-thermal X-ray source lies at the center of G76.9+1.0, lacks an optical counterpart, and anchors nebular emission consistent with a PWN. Most importantly, the pulsed flux detected using *RXTE* accounts for all of the *Chandra* emission and no more. These properties are consistent with pulsars producing broadband magnetospheric emission powered by rotational energy losses. *Chandra* astrometry thus locates the pulsar to sub-arcsec precision.

PSR J2022+3842 is outstanding in several respects. It is the second-most energetic Galactic pulsar known, after the Crab pulsar, and the fourth overall, taking into account two LMC pulsars, in N157B (PSR J0537−6910, with $\dot{E} = 4.9 \times 10^{38}$ erg s$^{-1}$ and $P = 16$ ms) and in SNR 0540−69 (PSR J0540−6919, with $\dot{E} = 1.5 \times 10^{38}$ erg s$^{-1}$ and $P = 50$ ms). However, it is among the least efficient at converting its spin-down luminosity into X-rays[1], with $\eta \equiv L_{2-10\,\mathrm{keV}}/\dot{E} = 5.9 \times 10^{-5}\,D_{10}^2$. The flat pulsed spectrum also sets it apart from the typical young, energetic pulsar, deviating significantly from the observed trend $\Gamma \propto 1/\sqrt{\dot{E}}$ (Gotthelf 2003; 2–10 keV), which predicts an index of $\Gamma = 1.8$. Flat power laws have primarily been found among pulsars with H.E.S.S. counterparts (e.g., PSR J1838−0655; Gotthelf & Halpern 2008).

PSR J2022+3842 is also the second-most rapidly rotating young pulsar after the LMC pulsar J0537−6910, and the shortest-period radio-bright pulsar known. Its ra-

---

[1] For ease of comparison with the compilation of Kargaltsev & Pavlov (2008), the flux, luminosity, and efficiency in the 0.5–8 keV band are $F_{\mathrm{PSR}} = 4.0 \times 10^{-13}$ ergs cm$^{-2}$ s$^{-1}$, $L_{\mathrm{X}} = 6.5 \times 10^{33}\,D_{10}^2$ ergs s$^{-1}$, and $L_{\mathrm{X}}/\dot{E} = 5.5 \times 10^{-5}\,D_{10}^2$.

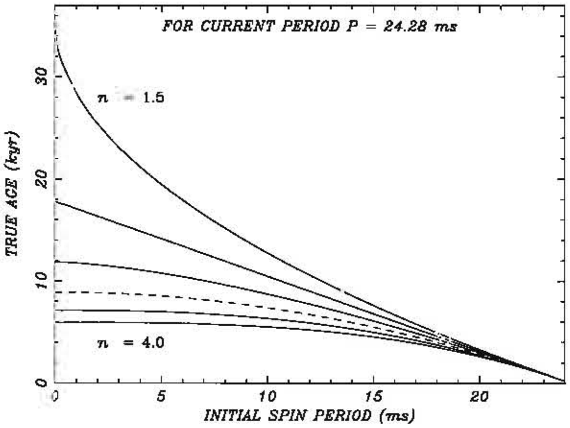

**Figure 5.** The true age $\tau$ of PSR J2022+3842 as a function of its spin period at birth, $P_0$, according to Equation (1); $n$ is the braking index. The curves correspond, from top to bottom, to $n$ = 1.5, 2.0, 2.5, 3.0 (dashed), 3.5, and 4.0, converging at the present-day period, $P = 24.28$ ms. The associated upper-limits on the pulsar age (for $P_0$ much smaller than $P$) are ~ 36, 18, 12, 9, 7, and 6 kyr, respectively.

dio properties are thus potentially interesting probes of the elusive radio emission mechanism in pulsars, but detailed studies will be hampered by this object's faintness and the interstellar propagation effects imposed by its great distance. The short rotation period also engenders uncertainty in the pulsar's (and thus the supernova remnant's) age: the characteristic age $\tau_c = P/2\dot{P} = 8.9$ kyr approximates the true age $\tau$ only when $P_0 \ll P$, where $P_0$ is the spin period at birth,

$$\tau = \frac{P}{(n-1)\dot{P}}\left[1-\left(\frac{P_0}{P}\right)^{n-1}\right], \qquad (1)$$

where $n$ is the so-called "braking index." For a birth period of 16 ms, the shortest known among young pulsars, the true age decreases to $\approx 5$ kyr, assuming spin-down due to magnetic dipole braking ($n = 3$). A countering effect, however, is spindown that deviates from the standard dipole assumption: the measured braking indices for several young pulsars are found to lie within the range $2.0 \lesssim n < 3.0$ (see, e.g., Melatos 1997). For example, as shown in Figure 5, $P_0 = 10$ ms for $n = 2$ would imply an age of 11 kyr. For any assumed value of $n$, an upper limit to the age of the pulsar, and thus the remnant, is provided in the limit $P_0 \to 0$. A braking index well below $n = 1.5$ would be highly unusual, so that $\sim 40$ kyr is a reasonable upper limit on the age of G76.9+1.0.

PSR J2022+3842 lacks the bright X-ray PWN expected from an energetic pulsar: it is only the second example (of some 20) of a pulsar with $\dot{E} \gtrsim 4 \times 10^{36}$ erg s$^{-1}$ unaccompanied by a PWN of comparable brightness, $F_{\rm PWN}/F_{\rm PSR} \gtrsim 1$, defying the trend presented in Gotthelf (2004). As such, it is similar to PSR J1617−5055 (Torii et al. 1998), the 69 ms pulsar with $\dot{E} = 1.6 \times 10^{37}$ erg s$^{-1}$, $B_s = 3.1 \times 10^{12}$ G, and $\tau_c = 8.1$ kyr. The underluminous PWNe in these cases remain unexplained. In other respects, however, the X-ray PWN around PSR J2022+3842 may not be so unusual. The semimajor axis of the elliptical elongation around the unresolved source is approximately 6″ in length, representing a physical dimension of $9 \times 10^{17}\ D_{10}$ cm. For comparison, the Vela PWN's X-ray "outer arc" lies at a distance $1 \times 10^{17}$ cm from the pulsar in the geometric model of Helfand et al. (2001).

If the extended emission around PSR J2022+3842 does arise from axisymmetric features, the *Chandra* image constrains—in analogy with the Crab, Vela, and others—the orientation of the pulsar's spin axis: in inclination, to $\simeq 50°$, and on the sky, to the symmetry axis at position angle $-64°$ North through East, orthogonal to the long direction of the diffuse X-ray emission and the ridge linking the radio lobes. The apparent alignment of spin axes and proper motion vectors in some of these same pulsars offers a testable prediction for the motion of PSR J2022+3842. The spin inclination relative to the line of sight, meanwhile, may help elucidate the role of viewing geometry (e.g., relative to a narrow magnetospheric emission beam) in *i)* producing simultaneously a narrow X-ray pulse but an unexpectedly broad radio pulse, a reversal of their typical relationship, and *ii)* determining whether the observed neutron star spectrum is primarily thermal or nonthermal: the flat spectrum of PSR J2022+3842 departs markedly from the dominant thermal emissions of the central stars in the Vela and DA 495 SNRs.

We have already alluded to some of the notable similarities between G76.9+1.0 and DA 495, both of which can now unambiguously be characterized as radio PWNe. Both are very bright radio sources without a well-defined outer boundary. Both manifest a bipolar structure and have a steep radio spectrum, unusual for a PWN. DA 495 has a break in its radio spectrum at roughly 1 GHz, and G76.9+1.0 may have one below that as well. Both show very faint X-ray emission compared to their radio emission, and a small X-ray nebula compared to the radio nebula. The conclusions arrived at by ASL+08 for DA 495 may thus also apply to G76.9+1.0. For example, based on the radio/X-ray PWN size ratio of DA 495, $\gtrsim 25$, and other lines of argument (see also Kothes et al. 2008), ASL+08 suggested that the pulsar wind energizing DA 495 has a high magnetization factor—i.e., it carries electromagnetic flux and particle flux at roughly comparable levels—in contrast with the Crab, which has a strongly particle-dominated wind, but similar to independent assessments of the wind properties of the Vela pulsar. Moreover, ASL+08 speculated that, because particle-dominated winds are necessary for efficient conversion of wind luminosity to synchrotron luminosity, PWNe in which Poynting flux is an important wind component may be those with dim X-ray PWNe.

The PWN size ratio for G76.9+1.0 is $\simeq 20$, comparable to DA 495 and nearly two orders of magnitude greater than that for the Crab Nebula. (At a distance of 10 kpc, G76.9+1.0 may be the largest PWN known in our Galaxy, with a physical size of 29 × 35 pc, bigger than or comparable to MSH 15−57, which is at least 25 pc in diameter, Gaensler et al. 2000, and so far believed to be the largest Galactic PWN.) If our prior conclusions hold, the wind from PSR J2022+3842 should be highly magnetized well beyond its termination shock, contributing to the low X-ray conversion efficiency of its PWN. Why this might be so is an open question.

The overarching conclusion of ASL+08 and

Kothes et al. (2008) was that DA 495 is likely to be a PWN of advanced age ($\sim$ 20 kyr), but having evolved without significant interaction with the ambient medium. All of the characteristics we find for G76.9+1.0 similarly indicate a rather old object, yet PSR J2022+3842 has all the characteristics of a young object: a spin-down age of 20 kyr would require both $n < 2$ and very high spin at birth, $P_0 \lesssim 5$ ms. We do not have a ready explanation for this apparent discrepancy, which highlights the importance of having uncovered the spin and energetic properties of the central pulsar.

G76.9+1.0 and its pulsar, J2022+3842, are clearly unusual and require further investigation. Additional multi-wavelength observations (e.g., an X-ray search for the SNR shell, to aid in constraining the system's age) may be fruitful in providing important components for their understanding. Based on its spin-down luminosity, and given the sub-arcsec localization and available timing information, PSR J2022+3842 is a good candidate for a search for gamma-ray pulsations using *Fermi* data. The absence of a bright PWN, however, makes it an unlikely TeV target, even though the spectrum of the pulsed X-ray emission suggests otherwise.

Support for this work was provided by the National Aeronautics and Space Administration through *Chandra* Award Number GO5-6077Z issued by the *Chandra* X-ray Observatory Center, which is operated by the Smithsonian Astrophysical Observatory for and on behalf of NASA under contract NAS8-03060. The National Radio Astronomy Observatory is a facility of the National Science Foundation operated under cooperative agreement by Associated Universities, Inc. We have also made use of *RXTE* data provided by the High Energy Astrophysics Archive at NASA's Goddard Space Flight Center, as well as data products from the Two Micron All Sky Survey, a joint project of the University of Massachusetts and the Infrared Processing and Analysis Center/Caltech, funded by NASA and the National Science Foundation. SSH acknowledges support by the Natural Sciences and Engineering Research Council of Canada (NSERC) and the Canada Research Chairs program.

## REFERENCES

Arzoumanian, Z., Safi-Harb, S., Landecker, T. L., Kothes, R., & Camilo, F. 2008, ApJ, 687, 505 (ASL+08)
Buccheri, R., et al 1983, A&A, 128, 245
Burke, B. E., Gregory, J., Bautz, M. W., Prigozhin, G. Y., Kissel, S. E., Kosicki, B. N., Loomis, A. H., & Young, D. J. 1997, IEEE Trans. Electron Devices, 44, 1633
Camilo, F. 2004, Young Neutron Stars and Their Environments, 218, 97
Cognard, I., Shrauner, J. A., Taylor, J. H., & Thorsett, S. E. 1996, ApJ, 457, L81
Cordes, J. M., & Lazio, T. J. W. 2002, arXiv:astro-ph/0207156
Dodson, R., Lewis, D., McConnell, D., & Deshpande, A. A. 2003, MNRAS, 343, 116
Gaensler, B. M., Dickel, J. R., & Green, A. J. 2000, ApJ, 542, 380
Gotthelf, E. V. 2003, ApJ, 591, 361
Gotthelf, E. V. 2004, in Young Neutron Stars and Their Environments, Ed. F. Camilo & B. M. Gaensler (San Fran., CA), IAU Symp. 214, 225
Gotthelf, E. V. & Halpern, J. P. 2008, ApJ, 681, 515
Helfand, D. J., Gotthelf, E. V., & Halpern, J. P. 2001, ApJ, 556, 380
Hotan, A. W., van Straten, W., & Manchester, R. N. 2004, PASA, 21, 302
Jahoda, K., Swank, J. H., Giles, A. B., Stark, M. J., Strohmayer, T., Zhang, W., & Morgan, E. H. 1996, Proc. SPIE, 2808, 59
Kaplan, D. L., et al. 2005, PASP, 117, 643
Kargaltsev, O., & Pavlov, G. G. 2008, 40 Years of Pulsars: Millisecond Pulsars, Magnetars and More, eds. C. Basa, A. Cumming, V. M. Kaspi, & Z. Wang, ASP Conf. Proc., 983, 171
Kothes, R., Reich, W., Foster, T., & Byun, D.-Y. 2003, ApJ, 588, 852
Kothes, R., Landecker, T. L., Reich, W., Safi-Harb, S., & Arzoumanian, Z. 2008, ApJ, 687, 516
Landecker, T. L., Higgs, L. A., & Wendker, H. J 1993, A&A, 276, 522
Li, J., Kastner, J. H., Prigozhin, G. Y., Schulz, N. S., Feigelson, E. D., & Getman, K. V. 2004, ApJ, 610, 1204
Melatos, A. 1997, MNRAS, 288, 1049
Mitra, D., & Deshpande, A. A. 1999, A&A, 346, 906
Moffett, D. A., & Hankins, T. H. 1999, ApJ, 522, 1046
Ord, S. M., van Straten, W., Hotan, A. W., & Bailes, M. 2004, MNRAS, 352, 804
Radhakrishnan, V., & Cooke, D. J. 1969, Astrophys. Lett., 3, 225
Ransom, S. M., Eikenberry, S. S., & Middleditch, J. 2002, AJ, 124, 1788
Roberts, M. S. E., Hessels, J. W. T., Ransom, S. M., Kaspi, V. M., Freire, P. C. C., Crawford, F., & Lorimer, D. R. 2002, ApJ, 577, L19
Rots, A. H., et al. 1998, ApJ, 501, 749
Safi-Harb, S., Matheson, H., & Kothes, R. 2011, 218th AAS meeting, Boston, MA (paper in preparation)
Torii, K., et al. 1998, ApJ, 494, L207
Wendker, H. J. 1991, Higgs, L. A, Landecker, T. L. 1991, A&A, 241, 551